High-Order/Low-Dissipation Chain-Rule Flux Solution Reconstruction Schemes in FUN3D

Emmett Padway*
NASA Langley Research Center, Hampton, VA 23681, USA
Hiroaki Nishikawa†
National Institute of Aerospace, Hampton, VA 23666, USA

In this paper, we report progress in the development of economically high-order flux-solution-reconstruction (FSR) schemes, which are second-order accurate on general unstructured grids but achieve high-order accuracy when a grid is regular. Two variants of the FSR schemes are discussed: chain-rule-flux-solution reconstruction (CFSR) and quadratic-form-flux-solution reconstruction (QFSR), where the former is based on the chain rule and the latter on the flux reconstruction expressed as a function of solution variables. These schemes are tested for flows with shock waves with a limiter incorporated in the flux and solution reconstructions. Improved results, compared with second-order methods, are demonstrated for inviscid and viscous flows with both smooth grids and adaptive grids.

1. Introduction

A widely used way of acheiving second-order spatial accuracy in finite volume (FV) discretization for computational fluid dynamics (CFD) codes are the Monotonic Upstream-centered Scheme for Conservation Laws (MUSCL) schemes[1] for structured grids or their unstructured counterparts called U-MUSCL schemes. A series of papers[2–6] have contained clarifications on the details of U-MUSCL-type unstructured-grid schemes and identified efficient flux-solution reconstruction (FSR) schemes that can achieve high-order accuracy on a regular quadrilateral/hexahedral grid away from a boundary. The FSR schemes are based on point-valued solutions and a point-valued approximation to a target system of equations, which can be either at a cell center or at a node in an unstructured grid. These schemes are efficient because they achieve high-order accuracy with only a single flux evaluation per face. This study follows the work of Nishikawa[5] and stores solutions at nodes and applies the edge-based flux quadrature formula to construct a point-valued approximation to the Euler and Navier-Stokes equations in a conservative manner. As demonstrated,[5] high-order accuracy is achieved on a regular grid by high-order solution and flux reconstruction techniques based on the U-MUSCL formula originally proposed by Burg[7] and later extended by Yang and Harris.[8] A unique feature of the FSR schemes is the flux reconstruction method used, which is critical to achieving high-order accuracy for nonlinear equations but has long been ignored in the U-MUSCL-type schemes. Another is the set of techniques to avoid computing and storing flux derivatives (which can be expensive in three dimensions): utilizing the chain rule in a solution-based quadratic flux reconstruction. Accuracy up to fifth-order has been demonstrated for simple smooth inviscid problems on regular grids.[5]

In this paper, we demonstrate the 3^{rd}- and 4^{th}-order FSR schemes in one- and two-dimensions, as well as in three dimensions in the FUN3D code developed at NASA Langley.[9] We look at truncation and discretization errors on regular triangular/tetrahedral and quadrilateral/hexahedral grids followed by an evaluation of these schemes on perturbed or irregular variants of these grids to better demonstrate the error properties of these respective schemes. We also show the behavior of these schemes on realistic geometries, showing improvements on irregular or adapted grids.

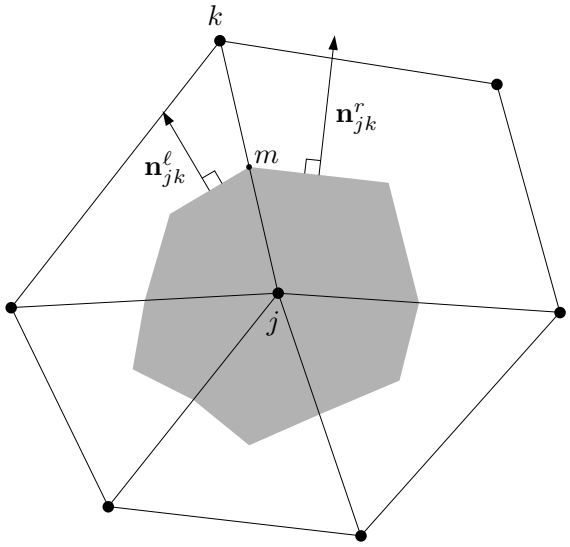

Figure 1. A stencil for the edge-based FSR schemes, $\mathbf{n}_{jk} = \mathbf{n}^\ell_{jk} + \mathbf{n}^r_{jk}$.

2. FSR Schemes

Consider a general system of hyperbolic equations:

$$\frac{\partial \mathbf{u}}{\partial t} + \mathrm{div}\mathcal{F} = \mathbf{s}, \tag{2.1}$$

where $\mathbf{u}$ is a vector of conservative variables, $\mathcal{F}$ is the flux tensor, and $\mathbf{s}$ is a forcing term. The FSR schemes are defined as a flux-balance discretization of Equation (2.1) based on the edge-based flux quadrature applied to a dual control volume around a node j in an unstructured grid (see Figure 1):

$$\frac{d\mathbf{u}_j}{dt} + \frac{1}{V_j} \sum_{k \in \{k_j\}} \Phi_{jk} |\mathbf{n}_{jk}| = \mathbf{s}_j, \tag{2.2}$$

with the following numerical flux

$$\Phi_{jk} = \frac{1}{2} \left[\mathbf{f}_L + \mathbf{f}_R \right] - \frac{1}{2} \hat{\mathbf{D}}_n \left[\mathbf{u}(\mathbf{w}_R) - \mathbf{u}(\mathbf{w}_L) \right], \tag{2.3}$$

where V_j is the dual volume around the node j, $\mathbf{f} = \mathcal{F} \cdot \hat{\mathbf{n}}_{jk}$ is the flux projected along the directed-area vector, which is the sum of all dual faces shared by the edge, $\mathbf{n}_{jk} = \hat{\mathbf{n}}_{jk} |\mathbf{n}_{jk}|$, $\hat{\mathbf{D}}_n = |\partial \mathbf{f} / \partial \mathbf{u}|$ is the dissipation matrix evaluated with the Roe averages of either the nodal values $\mathbf{w}_j$ and $\mathbf{w}_k$ for robustness and smoothness of the residual,[10,11] or the reconstructed values $\mathbf{w}_L$ and $\mathbf{w}_R$. The solution reconstruction[1] is performed with the primitive variables $\mathbf{w} = (\rho, \mathbf{v}, p)$ as

$$\mathbf{w}_L = \kappa \frac{\mathbf{w}_i + \mathbf{w}_k}{2} + (1 - \kappa) \left[\mathbf{w}_j + \widehat{\partial}_j \mathbf{w}_j \right] + \kappa_3 \, \widetilde{\partial}^3_j \mathbf{w}, \tag{2.4}$$

$$\mathbf{w}_R = \kappa \frac{\mathbf{w}_k + \mathbf{w}_j}{2} + (1 - \kappa) \left[\mathbf{w}_k + \widehat{\partial}_k \mathbf{w}_k \right] + \kappa_3 \, \widetilde{\partial}^3_k \mathbf{w}, \tag{2.5}$$

where

$$\widetilde{\partial}^3_j \mathbf{w} = \frac{1}{2} \left\{ \widehat{\partial}_j \mathbf{w}_k - \widehat{\partial}_j \mathbf{w}_j \right\} - \widehat{\partial}^2_j \mathbf{w}_j, \quad \widetilde{\partial}^3_k \mathbf{w} = \frac{1}{2} \left\{ \widehat{\partial}_k \mathbf{w}_j - \widehat{\partial}_k \mathbf{w}_k \right\} - \widehat{\partial}^2_k \mathbf{w}_k, \tag{2.6}$$

*Research Aerospace Engineer, Aeroelasticity Branch, emmett.m.padway@nasa.gov, Senior Member AIAA
†Research Fellow (hiro@nianet.org), 100 Exploration Way, Hampton, VA 23666 USA, Associate Fellow AIAA

$$\widehat{\partial}_j = (\mathbf{x}_m - \mathbf{x}_j)\cdot\nabla, \quad \widehat{\partial}_k = (\mathbf{x}_m - \mathbf{x}_k)\cdot\nabla, \tag{2.7}$$

$\mathbf{x}_m$ denotes the position vector of the edge midpoint, and $\mathbf{x}_j$ and $\mathbf{x}_k$ denote the nodal position vectors of j and its neighbor k, respectively (see Figure 1). As discussed previously,[5] the U-MUSCL of Burg corresponds to $\mathbf{f}_L = \mathbf{f}(\mathbf{w}_L)$ and $\mathbf{f}_R = \mathbf{f}(\mathbf{w}_R)$ with $\kappa = 1/2$ and $\kappa_3 = 0$, and the U-MUSCL scheme of Yang and Harris with $\kappa = 1/3$ and $\kappa_3 = -2/3$; these schemes cannot be higher than second-order accurate for nonlinear equations, in principle.[4,5]

Flux reconstruction is required to achieve third- and higher-order accuracy. We consider two efficient techniques: chain-rule-flux-solution reconstruction (CFSR) and quadratic-form-flux-solution reconstruction (QFSR) as proposed previously.[5] In CFSR, we perform the flux reconstruction by the chain rule:

$$\mathbf{f}_L = \theta\frac{\mathbf{f}_k + \mathbf{f}_j}{2} + (1-\theta)\left[\mathbf{f}_k + \widehat{\partial}_j\mathbf{f}_j\right] + \theta_3\,\widetilde{\partial}_j^3\mathbf{f}_j, \tag{2.8}$$

$$\mathbf{f}_R = \theta\frac{\mathbf{f}_k + \mathbf{f}_j}{2} + (1-\theta)\left[\mathbf{f}_k + \widehat{\partial}_k\mathbf{f}_k\right] + \theta_3\,\widetilde{\partial}_k^3\mathbf{f}_k, \tag{2.9}$$

where θ and θ_3 are parameters, and

$$\widetilde{\partial}_j^3\mathbf{f} = \frac{1}{2}\left\{\widehat{\partial}_j\mathbf{f}_k - \widehat{\partial}_j\mathbf{f}_j\right\} - \widehat{\partial}_j^2\mathbf{f}_j, \quad \widetilde{\partial}_k^3\mathbf{f} = \frac{1}{2}\left\{\widehat{\partial}_k\mathbf{f}_j - \widehat{\partial}_k\mathbf{f}_k\right\} - \widehat{\partial}_k^2\mathbf{f}_k, \tag{2.10}$$

$$\widehat{\partial}_j\mathbf{f}_j = \left(\frac{\partial\mathbf{f}}{\partial\mathbf{w}}\right)_j\widehat{\partial}_j\mathbf{w}_j, \quad \widehat{\partial}_k\mathbf{f}_k = \left(\frac{\partial\mathbf{f}}{\partial\mathbf{w}}\right)_k\widehat{\partial}_k\mathbf{w}_k, \tag{2.11}$$

$$\widehat{\partial}_j^2\mathbf{f}_j = \widehat{\partial}_j\left(\frac{\partial\mathbf{f}}{\partial\mathbf{w}}\right)_j + \left(\frac{\partial\mathbf{f}}{\partial\mathbf{w}}\right)_j\widehat{\partial}_j^2\mathbf{w}_j, \quad \widehat{\partial}_k^2\mathbf{f}_k = \widehat{\partial}_k\left(\frac{\partial\mathbf{f}}{\partial\mathbf{w}}\right)_k + \left(\frac{\partial\mathbf{f}}{\partial\mathbf{w}}\right)_k\widehat{\partial}_k^2\mathbf{w}_k. \tag{2.12}$$

The CFSR scheme is third-order accurate with,[5] $(\kappa, \kappa_3, \theta, \theta_3) = (arbitrary, 0, 1/3, 0)$, and fourth-order accurate with $(\kappa, \kappa_3, \theta, \theta_3) = (arbitrary, \kappa - 1, 1/3, 0)$ or $(\kappa, \kappa_3, \theta, \theta_3) = (arbitrary, \kappa - 1, 1/3, -8/15)$, which are referred to as CFSR3, CFSR4, and CFSR5, respectively. In these schemes, the choice of κ is arbitrary; it can be used to control the level of dissipation. Note that $\kappa = 1$ no longer means zero dissipation when $\kappa_3 \neq 0$.

On the other hand, in QFSR, we perform the flux reconstruction in terms of the solution:

$$\mathbf{f}_L = \mathbf{f}_j + \left(\frac{\partial\mathbf{f}}{\partial\mathbf{w}}\right)_j\Delta\mathbf{w}_L + \frac{\theta_2}{2}\left[\left(\frac{\partial^2\mathbf{f}}{\partial\mathbf{w}^2}\right)_j\Delta\mathbf{w}_L\right]\Delta\mathbf{w}_L, \tag{2.13}$$

$$\mathbf{f}_R = \mathbf{f}_k + \left(\frac{\partial\mathbf{f}}{\partial\mathbf{w}}\right)_k\Delta\mathbf{w}_R + \frac{\theta_2}{2}\left[\left(\frac{\partial^2\mathbf{f}}{\partial\mathbf{w}^2}\right)_k\Delta\mathbf{w}_R\right]\Delta\mathbf{w}_R, \tag{2.14}$$

where θ_2 is a parameter and

$$\Delta\mathbf{w}_L = \mathbf{w}_L - \mathbf{w}_j, \quad \Delta\mathbf{w}_R = \mathbf{w}_R - \mathbf{w}_k. \tag{2.15}$$

The QFSR scheme achieves, on a regular grid, third-order accuracy with $(\kappa, \kappa_3, \theta_2) = (1/3, 0, 2/3)$ and fourth-order accuracy with $(\kappa, \kappa_3, \theta_2) = (1/3, -2/3, 2/3)$. To achieve fifth-order accuracy, the solution reconstruction needs to be performed with the parameter vector and extra terms need to be introduced in the flux reconstruction; this scheme is called QFSR5(Z).[5]

3. Third-Order Truncation Error from Dissipation on Regular Triangular Grids

In this section, we show that a third-order truncation error term arising from the dissipation term cannot be completely eliminated on regular triangular grids. Since the averaged flux part of the numerical flux generates only even-order error terms, we focus on the dissipative part of the residual for a scalar conservation law with a variable u,

$$\frac{1}{V_j}\sum_{k\in\{k_j\}}\phi_{jk}^d|\mathbf{n}_{jk}|, \tag{3.1}$$

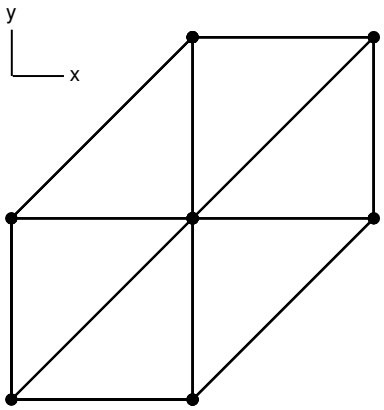

Figure 2. Regular triangular grid.

with

$$\phi_{jk}^d = -\frac{1}{2} D \left(u_R - u_L \right), \tag{3.2}$$

where D is taken as a global constant for simplicity and the gradients and the Hessian used in the reconstruction are assumed to be computed by the unweighted least squares (LSQ) method. Expanding this on a regular triangular grid as shown in Figure 2, we find

$$\begin{aligned} \frac{1}{V_j} \sum_{k \in \{k_j\}} \phi_{jk}^d |\mathbf{n}_{jk}| &= h^3 \frac{(\kappa_3 + 1 - \kappa) D}{12} \left(\sqrt{2} + \sqrt{5} \right) \left(\partial_{xxxx} u + \partial_{yyyy} u \right) \\ &+ h^3 \frac{D}{12} \left[\left(\frac{10(1-\kappa)}{3} + 4\kappa_3 \right) \sqrt{2} + \frac{2}{3}(1-\kappa)\sqrt{5} \right] \left(\partial_{xxxy} u + \partial_{xyyy} u \right) \\ &+ h^3 \frac{D}{12} \left[\left(\frac{14(1-\kappa)}{3} + 6\kappa_3 \right) \sqrt{2} + \frac{4}{3}(1-\kappa)\sqrt{5} \right] \partial_{xxyy} u. \end{aligned} \tag{3.3}$$

It is clear that the choice $\kappa_3 = \kappa - 1$, which eliminates a third-order error on a regular quadrilateral/hexahedral grid, cannot eliminate all the third-order error terms. But it eliminates the the first term and thus it can be a more accurate third-order scheme with $\kappa_3 = \kappa - 1$ than that with $\kappa_3 = 0$.

4. Limiting

So far, the FSR schemes have been demonstrated only for smooth flows.[5] These schemes need to be equipped with a nonoscillatory mechanism to be successfully applied to flows with shock waves. In this paper, we apply a limiter function $\psi_j \in [0, 1]$ to the solution reconstruction: e.g., for $\mathbf{w}_L$,

$$\mathbf{w}_L = \mathbf{w}_j + \psi_j \left[\overline{\nabla} \mathbf{w} \cdot (\mathbf{x}_{f_c} - \mathbf{x}_j) + \kappa \left\{ \frac{\mathbf{w}_k - \mathbf{w}_j}{2} - \overline{\nabla} \mathbf{w}_j \cdot (\mathbf{x}_{f_c} - \mathbf{x}_j) \right\} + \kappa_3 \widetilde{\partial_j^3} \mathbf{w} \right]. \tag{4.1}$$

where for the one- and two-dimensional problems in this paper we use the Venkatakrishnan limiter,[12] for the simulations in FUN3D, we use the R5 Nishikawa Limiter.[13] For the CFSR and QFSR schemes, the same limiter will be applied to the flux reconstruction. For high-order schemes, the Venkatakrishnan limiter is not suitable because it does not preserve third- and higher-order accuracy in smooth region and the Nishikawa limiter must be used (which preserves up to fifth-order accuracy), but numerical results show that the high-order schemes still produce improved results with the Venkatakrishnan limiter.

5. Numerical Results

In this paper, we present a one-dimensional shock wave calculation, a two-dimensional inviscid vortex problem and three-dimensional results on a variety of tetrahedral, hexahedral, and mixed prismatic-hexahedral grids simulated with the FUN3D code. In accuracy verification studies, we include another family of high-order schemes: U-MUSCL-SSQ3 and U-MUSCL-SSQ4. U-MUSCL-SSQ3 is a special third-order scheme derived in previous work,[14] which evaluates the left and right fluxes with the reconstructed solutions at $\kappa = 1/2$ with a special accuracy-preserving source quadrature formula. U-MUSCL-SSQ4 includes the extra term on the solution reconstruction with $\kappa 3 = \kappa - 1 = -1/2$.

5.1. Accuracy verification

In this section, we present accuracy verification results obtained for the Euler equations by the method of manufactured solutions on various types of grids. In all cases, the residual equations are solved by an implicit defect-correction solver with the exact Jacobian of the first-order residual (i.e., no LSQ gradients) relaxed by the Gauss-Seidel scheme. The Rusanov flux is employed here for robustness in the nonlinear solver and allows the solver to converge even with decreased dissipation from setting $\kappa = 3/4$. The iteration is taken to be converged when the residual is reduced by eight orders of magnitude in the L_1 norm. To focus on accuracy of the interior scheme, we specify the exact solution at boundary nodes, their neighbors, and the neighbors of the neighbors. The source term and its gradient are computed numerically and stored at each node and are used as part of the method of manufactured solutions to force the schemes to converge to the exact solution with grid refinement. For sections 5.1.1, 5.1.2, 5.1.3, and 5.1.4 an exact solution

$$\rho = 1.0 + 0.3\exp\left(\pi(0.3x + 0.3y)\right), \quad u = 0.15 + 0.3\exp\left(\pi(0.3x + 0.3y)\right), \tag{5.1}$$

$$v = 0.02 + 0.3\exp\left(\pi(0.3x + 0.3y)\right), \quad p = 1.0 + 0.3\exp\left(\pi(0.3x + 0.3y)\right), \tag{5.2}$$

is specified, whereas for section 5.1.5, the initial condition of the canonical inviscid vortex transport problem is itself an exact solution and needs no forcing term. The discretization error will be shown for the nondimensionalized pressure (results are similar for the other variables) and will be measured by the difference between the computed pressure and the pressure defned by the exact solution. Note that for the error convergence plots shown in the following section, $heff$ is the effective cell size, and is computed by the cube root of the quantity of the domain volume divided by the number of nodes.

5.1.1. Regular quadrilaterals

We first consider a series of regular quadrilateral grids with 1024, 2304, 4096, 6400, 9216, 12544, and 16384 nodes. Figure 3(a) shows the coarsest grid and the exact solution contours. The error convergence results are shown in Figure 3(b). As expected, CFSR4 and QFSR4 achieve fourth-order accuracy, and are significantly more accurate than their third-order versions, CFSR3 and QFSR3. Also as expected, U-MUSCL-SSQ3 and U-MUSCL-SSQ4 are second-order accurate and there is no advantage in U-MUSCL-SSQ4. U-MUSCL-YH is second-order accurate but more accurate than U-MUSCL with $\kappa = 0$ and $\kappa = 1/2$, as expected.

5.1.2. Regular equilateral triangles

Next, we consider regular equilateral triangular grids with 1024, 2304, 4096, 6400, 12544, and 16384 nodes. The coarsest grid is shown in Figure 4(a). Error convergence results are shown in Figure 4(b). Here, U-MUSCL-SSQ3 is third-order accurate as expected. U-MUSCL-SSQ4, CFSR4, QFSR4 are third-order accurate because of the dissipation term as discussed in Section 3. However, these schemes are significantly more accurate than their third-order versions. To demonstrate that these schemes are fourth-order without dissipation, we tested them with the dissipation term multiplied by 0.1. Results are indicated by (0.1D). As can be seen, the errors are further reduced and the convergence rates are very close to fourth-order, especially for QFSR4(0.1D) and U-MUSCL-SSQ4(0.1D).

5.1.3. Regular right-isosceles triangles

Next, we consider regular right-isosceles triangular grids with 1024, 2304, 4096, 6400, 12544, and 16384 nodes. The coarsest grid is shown in Figure 5(a). Error convergence results are shown in Figure 5(b). As

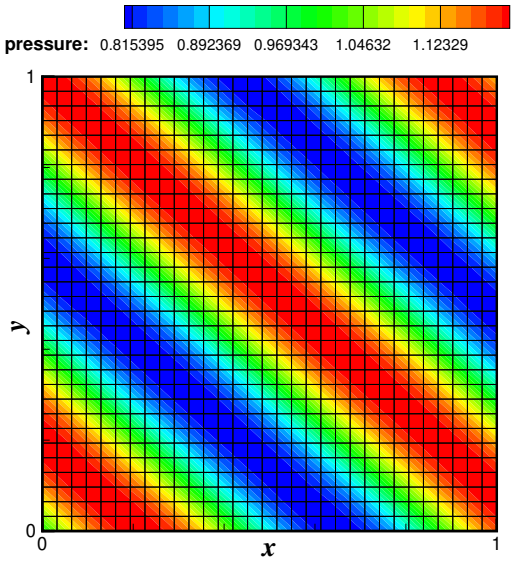

(a) The coarsest grid and the exact solution of nondimensionalized pressure.

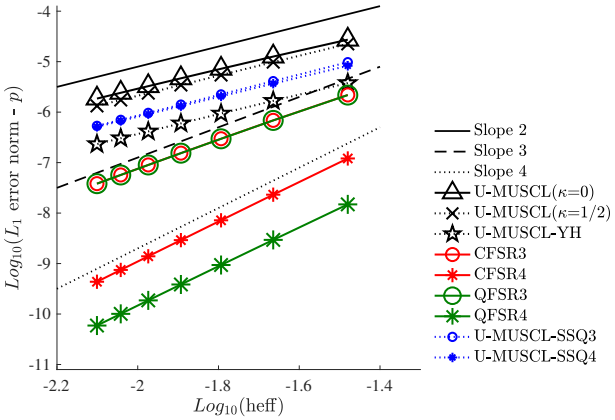

(b) Error convergence for the pressure.

Figure 3. Error convergence results for the Euler equations on regular quadrilateral grids.

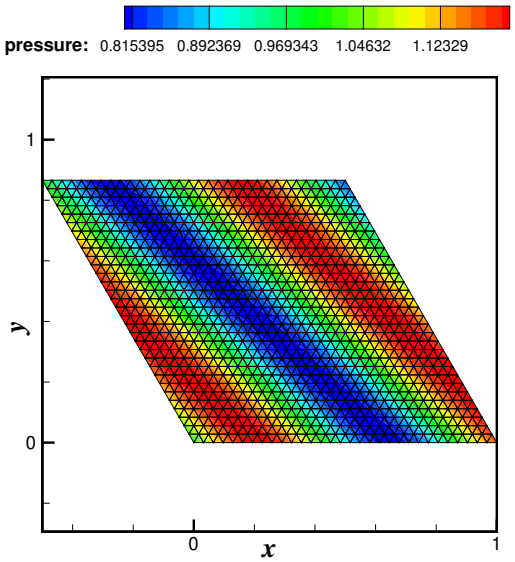

(a) The coarsest grid and the exact solution of nondimensionalized pressure.

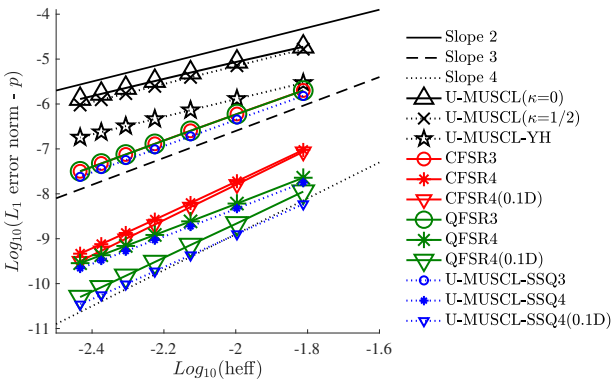

(b) Error convergence for the pressure.

Figure 4. Error convergence results for the Euler equations on equilateral triangular grids.

expected, the results are very similar to those for the equilateral triangular grids in the previous section. U-MUSCL-SSQ3 is third-order accurate, and U-MUSCL-SSQ4, CFSR4, QFSR4 are third-order accurate and significantly more accurate than their third-order counterparts.

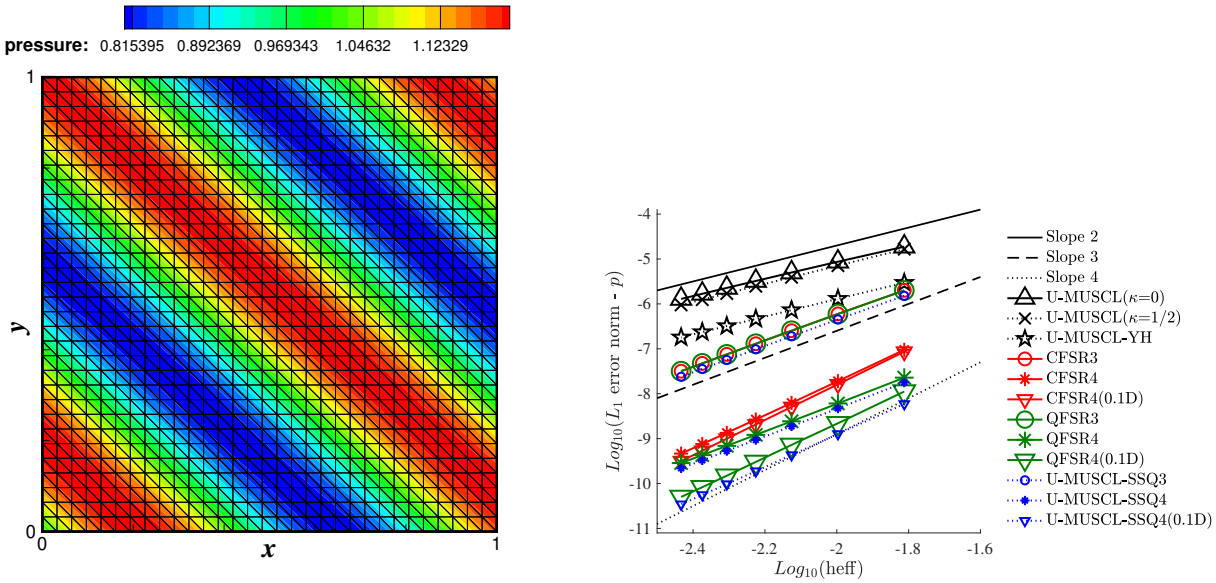

(a) The coarsest grid and the exact solution of nondimensionalized pressure.

(b) Error convergence for the pressure.

Figure 5. Error convergence results for the Euler equations on right triangular grids.

5.1.4. Irregular triangles

Next, we consider irregular triangular grids with 1024, 2304, 4096, 6400, 12544, and 16384 nodes. The coarsest grid is shown in Figure 6(a). Error convergence results are shown in Figure 6(b). In this case, no schemes achieve third-order accuracy. U-MUSCL-SSQ3 gives the lowest errors for all grids, which is consistent with results reported previously.[5,14] Also, for irregular grids, fourth-order versions are not necessarily more accurate than third-order versions. For example, U-MUSCL-SSQ3 is more accurate than U-MUSCL-SSQ4.

5.1.5. Fourth-order accuracy on regular triangular grids

Finally, to demonstrate fourth-order accuracy of CFSR4, QFSR4, and U-MUSCL-SSQ4 with zero dissipation on regular triangular grids, we consider an inviscid vortex transport problem shown in previous works.[5] The initial solution at $t = 0$ is shown in Figure 7(a). For the purpose of accuracy verification, it suffices to perform the calculation for a short time; we compute the solution at the final time $t_f = 1.0$ with the three-stage SSP Runge-Kutta scheme[15] (which is stable with zero dissipation) for the total of 1000 time steps with a constant time step $\Delta t = 0.001$, which is small enough for errors to be dominated by the spatial discretization. To verify the spatial order of accuracy, we perform the computation over a series of $n \times n$ regular triangular grids, where $n = 64, 80, 96, 112, 128$.

The initial pressure contours are shown on a coarse 16×16 grid in Figure 7(a). Error convergence results are shown in Figure 7(b). Zero dissipation versions are indicated by (0). As can be seen, CFSR4, QFSR4, and U-MUSCL-SSQ4 are fourth-order accurate with zero dissipation.

5.2. Shu-Osher Problem

We consider the Shu-Osher problem[16] with a uniform grid with 400 nodes. Results are shown in Figure 8 for a conventional second-order scheme (Fromm's scheme, $\kappa = 0$, $\kappa_3 = 0$), the U-MUSCL scheme of Yang and Harris (κ=1/3, κ_3=-2/3), and the QFSR4 scheme, where the Venkatakrishnan limiter is applied to all. The solid curve is a reference solution obtained with the QFSR4 scheme on a 1,600-node grid. As can

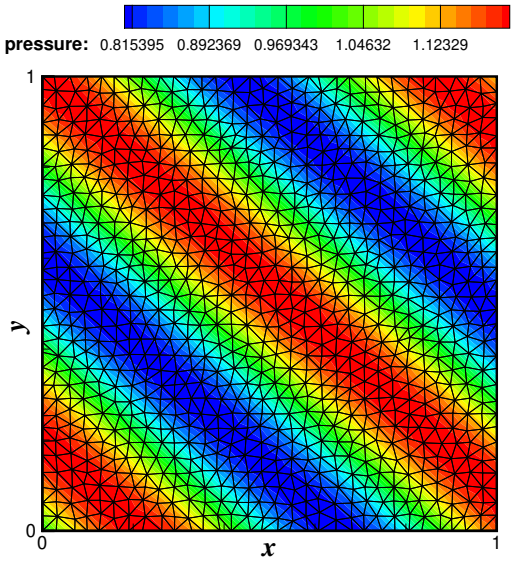

(a) The coarsest grid and the exact solution of nondimensionalized pressure.

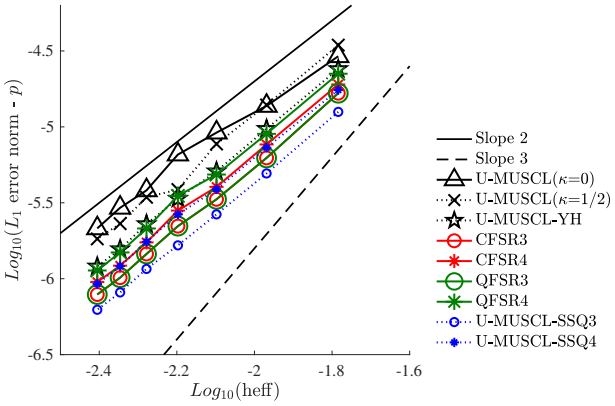

(b) Error convergence for the pressure.

Figure 6. Error convergence results for the Euler equations on irregular triangular grids.

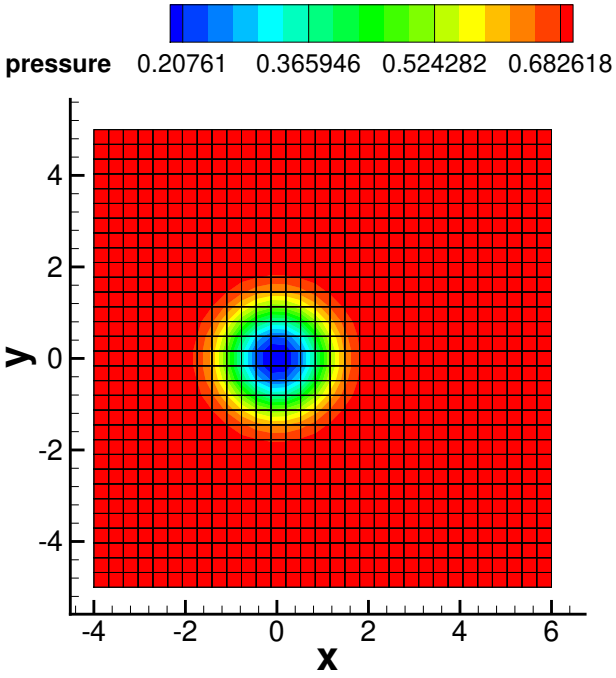

(a) The coarsest grid and the exact solution of nondimensionalized pressure.

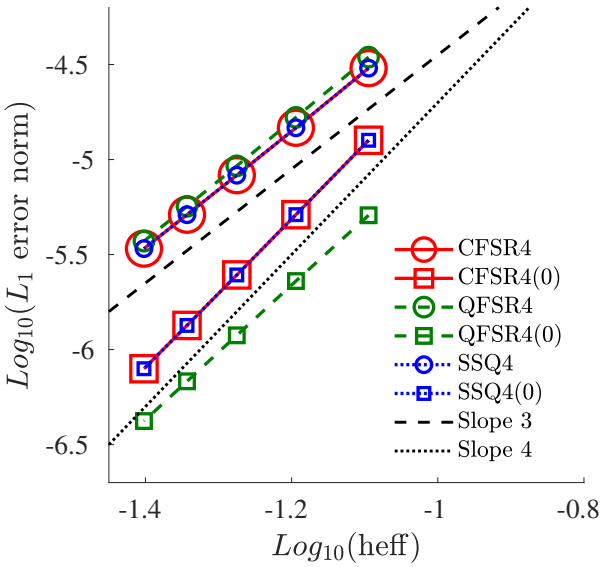

(b) Error convergence for the pressure.

Figure 7. Error convergence study for the unsteady Euler equations in two dimensions.

be seen, Fromm's scheme is the most dissipative, U-MUSCL-YH shows improved resolution, and QFSR4 achieves even higher resolution. These results indicate the importance of genuine high-order accuracy as U-MUSCL-YH is in fact restricted to second-order accuracy for nonlinear partial differential equations.[3,17]

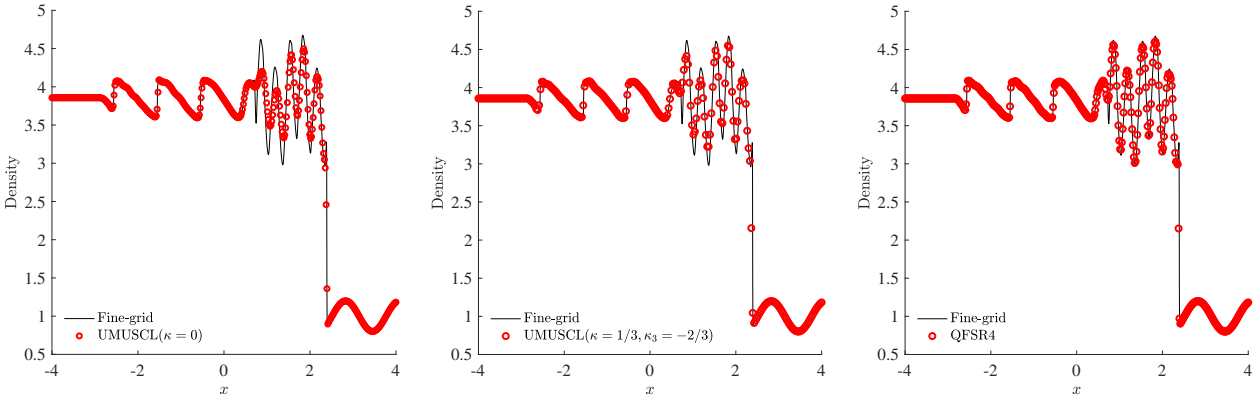

(a) U-MUSCL(κ=0, κ_3=0): Fromm. (b) U-MUSCL(κ=1/3, κ_3=-2/3).[8] (c) QFSR4.

Figure 8. Results for the Shu-Osher problem.

5.3. Inviscid Vortex Transport

We consider an inviscid vortex transport problem where the parameter K in the inviscid vortex solution is taken to be 6.0 to avoid linearization of the problem.[4] The initial solution is shown in Figure 9(a). The vortex travels to the right at $M_\infty = 0.5$ from $x = 0$ to $x = 10$. The grid is a regular quadrilateral grid with 65x129 nodes.

The final solutions are compared in Figure 9(b). As can be seen, the U-MUSCL scheme dissipates the solution by nearly the same amount for both (κ=0, κ_3=0) and (κ=1/3, κ_3=-2/3), which are both second-order accurate, in theory. On the other hand, the QFSR4 scheme is a fourth-order scheme and gives much better resolution. Again, it indicates the importance of high-order accuracy for nonlinear governing equations. Finally, the fifth-order QFSR5(Z) scheme produces an even more accurate solution.

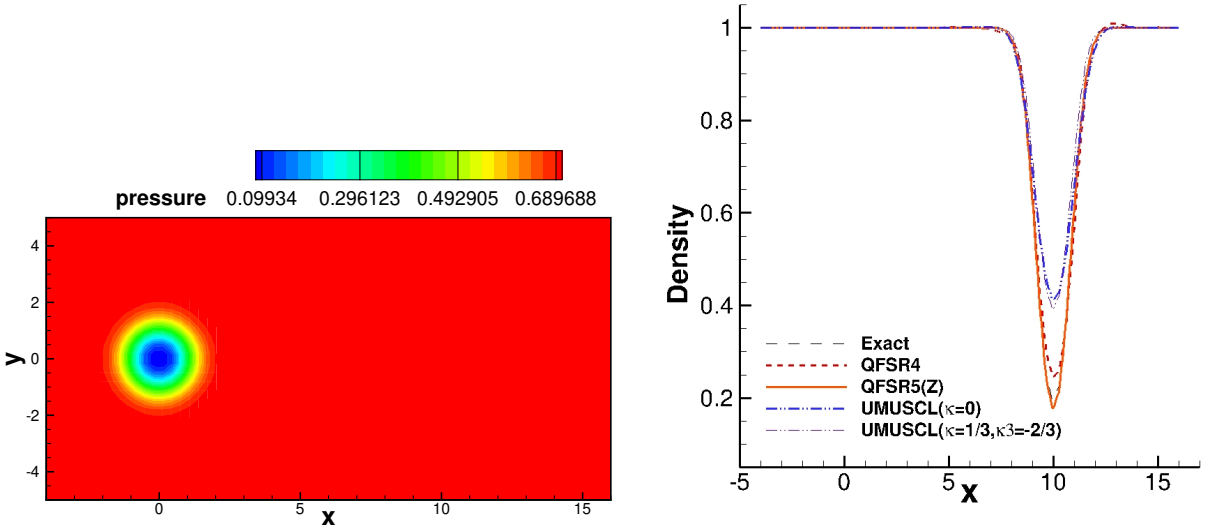

(a) Initial solution of nondimensionaled pressure. (b) Comparison of section plot at $y = 0$.

Figure 9. Results for the inviscid vortex transport problem.

5.4. FUN3D results

5.4.1. Truncation Error Verification

In this section, we present results from the FSR implementations inside FUN3D. Figure 10 contains results obtained for the Euler equations by the method of manufactured solutions on regular tetrahedral and hexahedral grids using the FSR schemes in FUN3D. The truncation error is analyzed at nodes with purely interior schemes (nodes 3 edges from the boundary) to verify proper implementation of the residual and source term, as we don't have access to a high order boundary closure. In the figure, the expected behavior is observed on the hexahedral grid, and on the tetrahedral grid error convergence is faster than expected. While it has been proven that these schemes cannot be 3rd-order (or higher) accurate in space on tetrahedral grids, this could be due to the comparatively small dissipative error that is left as the CFSR and QFSR schemes eliminate the larger source of 3rd-order error.

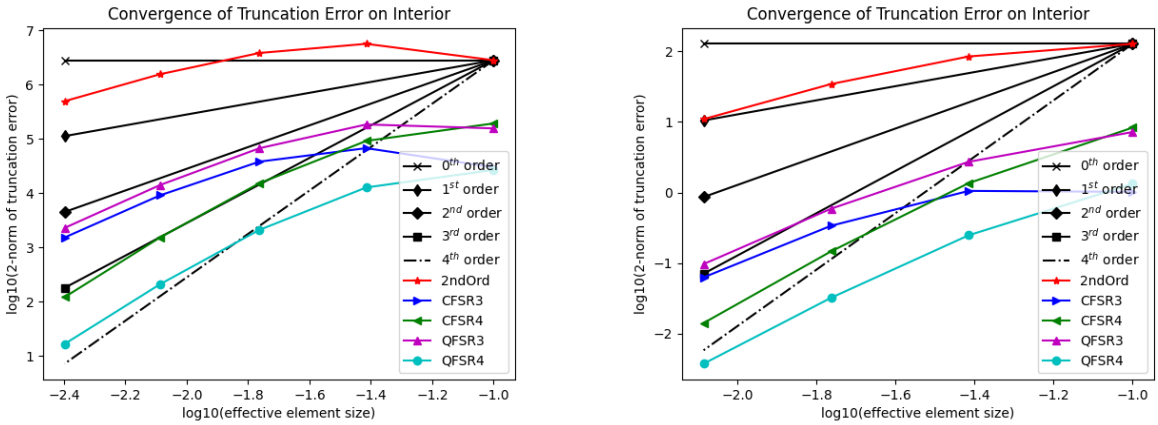

(a) TE convergence on hexahedral mesh.

(b) TE convergence on tetrahedral mesh.

Figure 10. Truncation error convergence on 8^3, 16^3, 32^3, 64^3, and 128^3 meshes

5.4.2. Hemisphere-Cylinder in Zero Angle-of-Attack Flow

The CFSR and QFSR schemes lose their order of accuracy properties on irregular grids but maintain lower dissipation through a smaller jump term in the dissipation term. In order to investigate this and the impact on integrated quantities, we consider a steady hemisphere-cylinder test case, as developed in the Turbulence Modeling Resource (TMR) and its associated papers.[18,19] This case is a RANS simulation with freestream Mach number 0.6 and zero angle-of-attack. The freestream unit Reynolds number per foot is 4.2×10^6, the radius of the hemisphere is 0.5, and the hemisphere-cylinder geometry has length 10. Further details of the flow condition and the geometry can be found from the work concering the grid generation codes,[20] and relevant reference and solution data are available at the NASA TMR website.[18] The focus here is on the values of the lift and drag coefficients on the finest regular mixed-element grids with prisms and hexahedra and with 71,368,353 nodes (a coarsened version with an arrow depicting the direction of flow is in Figure 11). Table 1 shows the values of the coefficients of lift and drag on the finest grid in the TMR sequence along with the wall time normalized by the cost of the U-MUSCL scheme. Note that the exact solution should have zero lift, so error is measured by the magnitude of the coefficient of lift. The QFSR4/CFSR4 schemes outperform their respective third-order accurate counrterparts which in turn outperform the default U-MUSCL scheme in FUN3D. This shows the improvement from using the low-dissipation formulations.

Having shown good behavior on a regular grid (with minimal additional cost), demonstrated by the order of magnitude lower drag for the QFSR4/CFSR4 schemes as compared to the default U-MUSCL one, we move to a demonstration of the low-dissipation schemes on irregular grids, these ones created through use of the *refine* software developed at NASA Langley.[21,22] These cases were run using pyrefine,[23] a python wrapper for the *refine* software, using the pyrefine controller to control the refinement, in this case doubling the complexity every 10 iterations. The full history of the adaptation for all schemes is in Figure 12, and shows

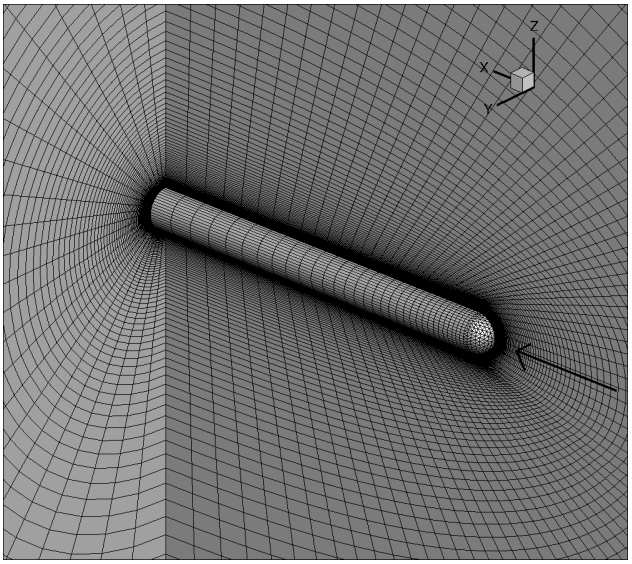

Figure 11. Coarsened (147k nodes) version of fine mesh

Table 1. Comparison of engineering coefficients on hemisphere-cylinder in zero angle-of-attack flow.

	Time	c_L	c_D
U-MUSCL($\kappa = 1/2$)	1.0	0.3612491204E-05	0.6330284789E-03
CFSR3	1.0425	0.3027483497E-05	0.6323746253E-03
CFSR4	1.0584	-0.3342316273E-06	0.7317624670E-03
QFSR3	1.15	0.8276169361E-05	0.5571458268E-03
QFSR4	1.095	0.4820069248E-07	0.7081040356E-03

that the U-MUSCL (denoted by 2ndOrder) and QFSR3/CFSR3 schemes are much more oscillatory in the integrated quantities from grid to grid as opposed to the QFSR4/CFSR4 schemes which are more consistent with mesh refinement, indicating that measures of interpolation error are more consistent grid to grid. Figure 12(b) just shows the FSR4 schemes and we can see that they appear to converge to their final quantity of c_D at approximately a third of the complexity required by the U-MUSCL scheme. Additionally CFSR4 is remarkably consistent from grid to grid indicating that in addition to the benefit it provides in having tunable dissipation, it also allows for more consistent refinement – due to more consistent interpolation error– allowing for high-fidelity simulations at lower cost.

5.4.3. Supersonic Bump

This supersonic bump is run at $M = 2.0$ for the Euler governing equations, with the goal being to evaluate the utility and behavior of these schemes for highly nonlinear shocked flows. The computational domain for this case was bounded within $(x, y, z) \in (0, 2) \times (0, 1) \times (-0.5, 0.5)$, and Figure 13 contains contour plots of the Mach number in the domain. The unstructured and perturbed triangular mesh consists of 45,000 nodes (on each 2D plane). The upper and lower boundaries are inviscid walls with farfield and symmetry boundary conditions being used in the x and y directions, respectively. This computational setup mimics that of previous work,[13,24] and further details on the geometry and limiter (Nishikawa's 5th order limiter) can be found in those papers.

Figure 13 appears to show that the QFSR4 scheme is slightly more oscillatory than the CFSR4 scheme, so it is helpful to look at a plot of the Mach number on the center line of the domain to see variations in the Mach number due to shocks and flow conditions. Figure 14 shows a comparison of centerline density between the FSR schemes and the FUN3D default U-MUSCL scheme. Figure 14(b) shows that the first

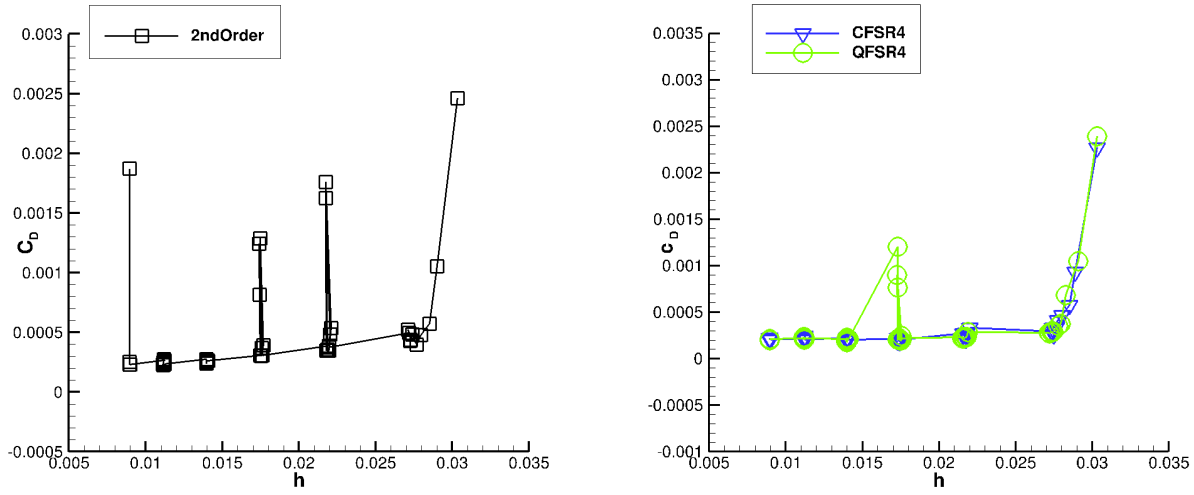

(a) Adaptation history of U-MUSCL

(b) CFSR4 and QFSR4 Schemes

Figure 12. Adaptation Cycle history.

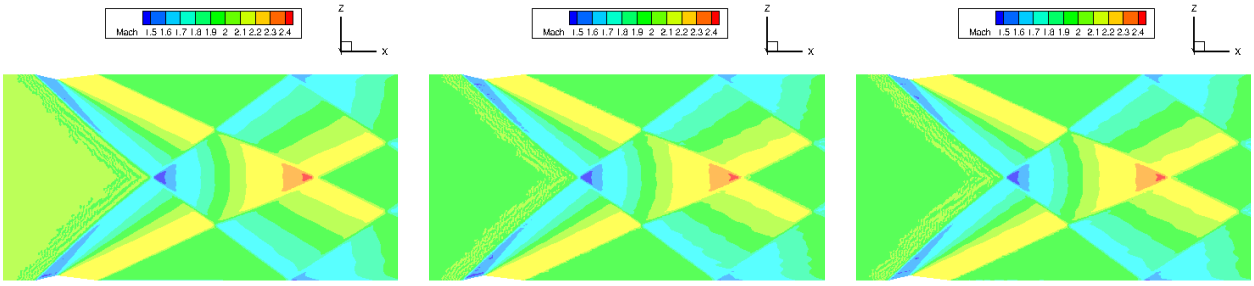

(a) 2nd Order

(b) CFSR4

(c) QFSR4

Figure 13. XZ plane of contours of Mach Number.

shock is better captured for the FSR4 schemes, with both CFSR schemes outperforming QFSR4 in capturing the highest peak value of Mach number, but with QFSR3 performing almost identically to the default U-MUSCL scheme. 14(c) shows the downside to the QFSR4 scheme in that it has much stronger oscillations, and CFSR4 is in fact the least oscillatory scheme. This seems to show that CFSR4 should be the desired scheme for transonic and supersonic flows due to its ability to more accurately capture the highest peak and suffering from less oscillatory behavior.

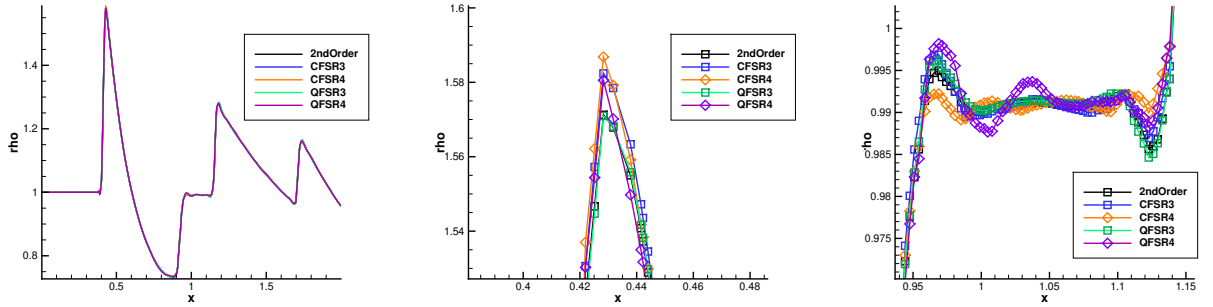

(a) Full domain view (b) First shock zoomed view (c) Oscillatory region zoomed view

Figure 14. Density as a function of x.

5.4.4. Cylinder in Unsteady Cross Flow

Finally, we look at FSR schemes on the semirealistic geometry of an infinite cylinder in cross flow. This case has $M = .1, Re_D = 3900$ and freestream temperature $T_{ref} = 460.0R$. The cylinder has diameter 1.0 and a spanwise length of 2.0, with an outer boundary located at approximately a of distance 100 units from the center of the cylinder. The domain is taken as periodic at the two XZ-planes with minimum and maximum y-coordinates. The grid used for these simulations is a mixed grid with prismatic and hexahedral cells, as shown in Figure 15. It has 3,934,800 nodes, 1,175,000 prisms, and 3,243,000 hexahedra. Simulations were run with the Roe flux, the Green-Gauss viscous discretization, and the second-order backward-difference time-steppping scheme with a nondimensionalized time step of 0.05 for 10,000 time steps, with 400 cores. At each physical time step, we perform 20 nonlinear iterations at maximum. Snapshots of the flow are in Figures 16 and 17. We can see the significant gains from moving from the second-order U-MUSCL schemes to the CFSR4 and QFSR4 schemes in the increased capturing of the smaller flow structures near the leeside of the cylinder. Here we see the gains on a benchmark unsteady case in capturing of physics that the higher dissipation schemes cannot achieve.

6. Conclusions and Future Work

The FSR schemes have been implemented and validated in standalone codes to verify correctness and implemented and benchmarked in the FUN3D code developed at NASA Langley. We have verified correctness through the use of MMS, and showed better capturing of physics using these low-dissipation schemes as opposed to the default U-MUSCL scheme with small additional computationl overhead. It seems that for realistic cases there is a significant benefit to using the CFSR4/QFSR4 schemes over the CFSR3/QFSR3/U-MUSCL schemes. Furthermore, while the QFSR4 scheme appears to be more accurate for smooth flows on regular grids, the CFSR4 scheme should be prefered due to the lack of oscillatory behavior for supersonic flow and the consistent interpolation error on adaptive meshes. Future work on this topic has begun as we have begun porting these schemes over to the GPU implementation of FUN3D, and efforts to repurpose these schemes for improved viscous schemes is the natural following step.

Acknowledgments

Part of this work was supported by the U.S. Army Research Office under the contract/grant number W911NF-19-1-0429.

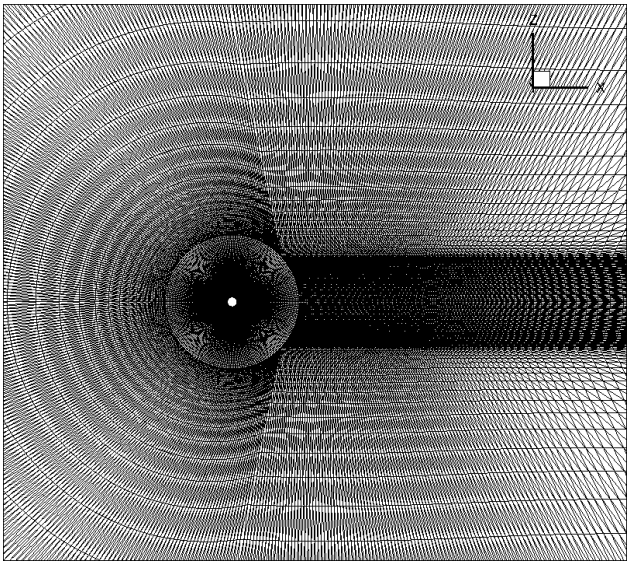

Figure 15. XZ plane of mesh.

References

[1]van Leer, B., "Towards the Ultimate Conservative Difference Scheme. V. A Second-Order Sequel to Godunov's Method," *Journal of Computational Physics*, Vol. 32, No. 1, 1979, pp. 101–136.

[2]Nishikawa, H., "A Truncation Error Analysis of Third-Order MUSCL Scheme for Nonlinear Conservation Laws," *International Journal for Numerical Methods in Fluids*, Vol. 93, No. 4, 2021, pp. 1031–1052.

[3]Nishikawa, H., "The QUICK Scheme is a Third-Order Finite-Volume Scheme with Point-Valued Numerical Solutions," *International Journal for Numerical Methods in Fluids*, Vol. 93, No. 7, 2021, pp. 2311–2338.

[4]Nishikawa, H., "On False Accuracy Verification of UMUSCL Scheme," *Communications in Computational Physics*, 2020.

[5]Nishikawa, H., "Economically High-Order Unstructured-Grid Methods: Clarification and Efficient FSR schemes," *International Journal for Numerical Methods in Fluids*, Vol. 93, No. 11, 2021, pp. 3187–3214.

[6]Padway, E. and Nishikawa, H., "Resolving Confusions over Third-Order Accuracy of U-MUSCL," *AIAA Scitech 2021 Forum*, AIAA Paper 2021-0056, Virtual Event, 2021.

[7]Burg, C. O. E., "Higher Order Variable Extrapolation for Unstructured Finite Volume RANS Flow Solvers," AIAA Paper 2005-4999, 2005.

[8]Yang, H. Q. and Harris, R. E., "Development of Vertex-Centered High-Order Schemes and Implementation in FUN3D," *AIAA Journal*, Vol. 54, 2016, pp. 3742–3760.

[9]Anderson, W. K., Biedron, R. T., Carlson, J.-R., Derlaga, J. M., Jr., C. T. D., Gnoffo, P. A., Hammond, D. P., Jacobson, K. E., Jones, W. T., Kleb, B., Lee-Rausch, E. M., Nastac, G. C., Nielsen, E. J., Padway, E., Park, M. A., Rumsey, C. L., Thomas, J. L., Thompson, K. B., Walden, A. C., Wang, L., Wood, S. L., and Wood, W. A., "FUN3D Manual: 14.0.2," Tech. Rep. NASA/TM–20230004211, NASA Langley Research Center, Hampton, Virginia, November 2023.

[10]Roe, P. L., "Approximate Riemann Solvers, Parameter Vectors, and Difference Schemes," *Journal of Computational Physics*, Vol. 43, 1981, pp. 357–372.

[11]Nishikawa, H., "Robust Numerical Fluxes for Unrealizable States," *Journal of Computational Physics*, Vol. 408, 2020, pp. 109244.

[12]Venkatakrishnan, V., "Convergence to Steady State Solutions of the Euler Equations on Unstructured Grids with Limiters," *Journal of Computational Physics*, Vol. 118, 1995, pp. 120–130.

[13]Nishikawa, H., *New Unstructured-Grid Limiter Functions*.

[14]Padway, E. and Nishikawa, H., "Resolving Confusions over Third-Order Accuracy of Unstructured MUSCL," *AIAA Journal*, Vol. 60, No. 3, 2022, pp. 1415–1439.

[15]Gottlieb, S., Shu, C.-W., and Tadmor, E., "Strong Stability-Preserving High-Order Time Discretization Methods," Vol. 43, No. 1, 2001, pp. 89–112.

[16]Shu, C.-W. and Osher, S. J., "Efficient Implementation of Essentially Non-Oscillatory Shock-Capturing Schemes," *Journal of Computational Physics*, Vol. 77, 1988, pp. 439–471.

[17]Zhang, R., Zhang, M., and Shu, C.-W., "On the Order of Accuracy and Numerical Performance of Two Classes of Finite Volume WENO Schemes," *CCP*, Vol. 9, No. 3, 2011, pp. 807–827.

[18]Rumsey, C. L., "Turbulence Modeling Resource," `https://turbmodels.larc.nasa.gov`, Accessed: 2023-11-22.

[19]Diskin, B., Anderson, W. K., Pandya, M. J., Rumsey, C. L., Thomas, J., Liu, Y., and Nishikawa, H., "Grid Convergence for Three Dimensional Benchmark Turbulent Flows," .

[20]Nishikawa, H. and Diskin, B., "Customized Grid Generation Codes for Benchmark Three-Dimensional Flows," .

[21]"Refine Repository," `https://github.com/nasa/refine`, Accessed: 2020-06-08.

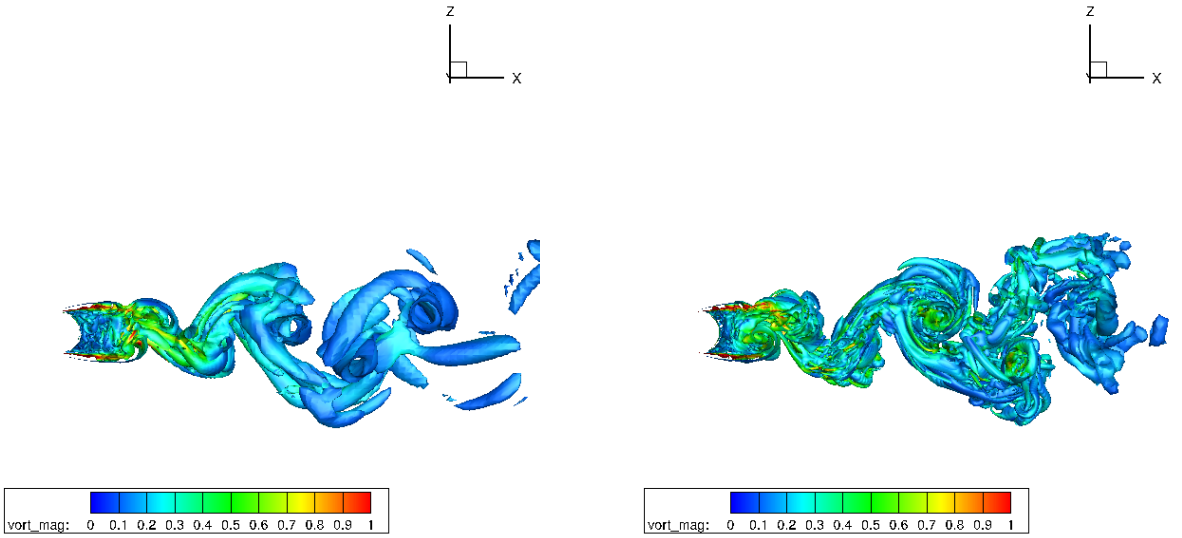

(a) U-MUSCL ($\kappa = 1/3$)

(b) U-MUSCL ($\kappa = 1/2$)

(c) CFSR4 ($\kappa = 1/2$)

(d) QFSR4 ($\kappa = 1/3$)

Figure 16. Horizontal view of isocontours of q-criterion colored by vorticity.

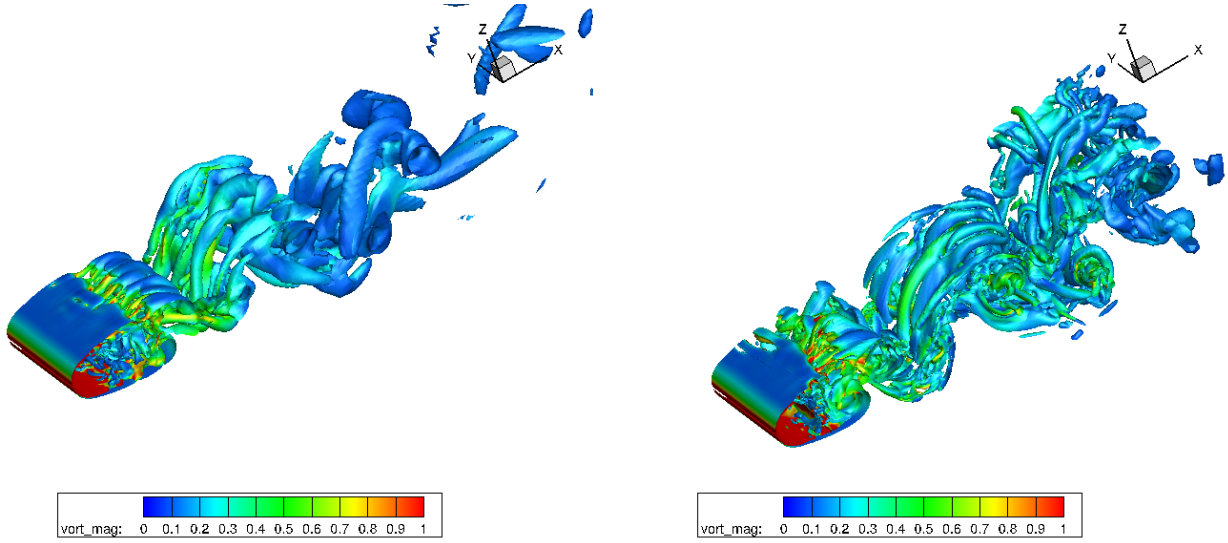

(a) U-MUSCL ($\kappa = 1/3$)

(b) U-MUSCL ($\kappa = 1/2$)

(c) CFSR4 ($\kappa = 1/2$)

(d) QFSR4 ($\kappa = 1/3$)

Figure 17. Isoparametric view of isocontours of q-criterion colored by vorticity.

[22]Park, M. A., *Anisotropic Output-Based Adaptation with Tetrahedral Cut Cells for Compressible Flows*, Ph.D. thesis, Massachusetts Institute of Technology, Sept. 2008.

[23]Jacobson, K. E., "pyrefine," `https://nasa.github.io/pyrefine`, Accessed: 2023-11-22.

[24]Ahmad, N. N., Park, M. A., Nishikawa, H., Wang, L., and Elmiligui, A. A., *Evaluation of Limiter Functions for Supersonic Applications*.